Available online at www.keaipublishing.com/en/journals/journal-of-magnesium-and-alloys/

ScienceDirect

Journal of Magnesium and Alloys 13 (2025) 5421–5437

www.elsevier.com/locate/jma

Full Length Article

Tension-compression asymmetry of an AM magnesium alloy unveiled by in-situ synchrotron X-ray diffraction ☆

Hao Chen [a,b], Huicong Chen [a], Yuanding Huang [c], Weimin Gan [d], Emad Maawad [d], Weidong Xie [b,*], Guobing Wei [b], Yan Yang [b], Yu Zou [a,*]

[a] *Department of Materials Science and Engineering, University of Toronto, 184 College Street, Toronto, M5S 3E4, Canada*
[b] *National Engineering Research Center for Magnesium Alloys, Chongqing University, Chongqing, 400044, China*
[c] *Institute of Metallic Biomaterials, Helmholtz-Zentrum Hereon, Max-Planck Str. 1, Geesthacht, 21502, Germany*
[d] *Institute of Materials Physics, Helmholtz-Zentrum Hereon, Max-Planck Str. 1, Geesthacht, 21502, Germany*

Received 9 August 2025; received in revised form 19 September 2025; accepted 1 October 2025
Available online 2 November 2025

Abstract

Magnesium (Mg) alloys typically exhibit anisotropic mechanical behaviors due to their hexagonal close-packed (hcp) crystal structures, often leading to tension-compression asymmetries. Understanding of the asymmetrical and related deformation mechanisms is crucial for their structural applications, particularly in the lightweight transportation industries. Nevertheless, the underlying deformation mechanisms (e.g., slip *versus* twinning) at each deformation stage during tension and compression have not been fully understood. In this study, we employed tensile and compressive tests on extruded Al and Mn containing Mg alloy, i.e., an AM alloy Mg-0.6Mn-0.5Al-0.5Zn-0.4Ca, during the synchrotron X-ray diffraction. Our results show that distinct deformation behaviors and mechanisms in tension and compression are associated with the strong texture in the extruded samples: (i) The tensile deformation is dominated by dislocation slips, with activation of non-basal ⟨a⟩ and ⟨c + a⟩ slip, but deformation twinning is suppressed. (ii) The compressive deformation shows early-stage tensile twinning, followed by dislocation slips. Twinning induces grain reorientation, leading to significant lattice strain evolution aligned with the texture. The pronounced tension-compression asymmetry is attributed to the favorable shear stress direction formed in the twinning system during compression, which facilitates the activation of tensile twins. During tension, the strain hardening rate (SHR) drops significantly after yielding due to limited activated slip systems. In contrast, the samples under compression exhibit significant increases in SHR after yielding. During compression, dislocation multiplication dominates the initial strain hardening, while twinning progressively contributes more significantly than dislocation slip at higher strains. This study improves our understanding of the tension-compression and strain hardening asymmetries in extruded AM Mg alloys.

Keywords: Mg alloy; Plastic deformation; Dislocation; Twinning; Synchrotron X-ray diffraction.

1. Introduction

Mg alloys are widely recognized for their low density, high strength-to-weight ratio, and excellent damping properties, making them attractive for the automotive and aerospace applications [1–4]. Nevertheless, the widespread use of Mg alloys as structural materials remains limited due to a number of inherent challenges, including limited plasticity, strong deformation anisotropy, and low absolute strength, particularly under complex loading conditions [5–8]. Their relatively poor formability and high anisotropy are associated with their hcp structure and a limited number of primary slip systems for plastic deformation [9–12]. Therefore, the enhancement of the ductility and a better understanding of the deformation anisotropy in Mg alloys are critical for their engineering applications in high-performance structural components.

☆ Peer review under the responsibility of Chongqing University.

* Corresponding authors.
E-mail addresses: wdxie@cqu.edu.cn (W. Xie), mse.zou@utoronto.ca (Y. Zou).

https://doi.org/10.1016/j.jma.2025.10.008

Alloying has been proven effective in improving the mechanical properties of Mg alloys by refining grains and precipitation strengthening [13–15]. Rare-earth-free Mg alloys have attracted growing interest due to their cost-effectiveness [16], for example, Mg alloys incorporating Ca, Zn, Al, and Mn [17–19]. Among them, the Mg-Mn-Al-Ca-Zn alloy distinguishes itself with an optimal balance of high strength and exceptional ductility due to its fine-grained microstructure and uniformly distributed nano-precipitates [20–22]. For example, Mg-Zn-Ca-Al-Mn alloy processed by equal-channel angular pressing which exhibits excellent ductility and thermal stability [23], due to the segregation of Zn and Ca elements at grain boundaries and the formation of β-Mn particles precipitates. Additionally, the fine precipitates inhibit dynamic recrystallization growth during extrusion, promoting the development of ultrafine grains. However, this new Mg-Mn-Al-Ca-Zn alloy exhibits a noticeable tension-compression asymmetry, and its related deformation mechanism is not well understood.

The high tension-compression asymmetry in Mg alloys [24] mainly results from the combined effects of the polar nature of deformation twinning and pronounced texture induced by thermomechanical processing [25,26]. For example, wrought Mg alloys typically develop a pronounced texture, with {0002} planes of most grains parallel to the processing direction [27,28]. During compression along this direction, tension twins with high Schmid factors and low critical resolved shear stress (CRSS) are readily activated, leading to a lower compressive yield strength (CYS) [24,29]. In contrast, the c-axes are subjected to compressive stress during tension, placing tension twins in a hard orientation and leading to a higher tensile yield strength (TYS) [30]. Therefore, the tension-compression asymmetry can be improved by weakening the texture or suppressing the activation of twinning during deformation [31,32]. It is reported that grain refinement in the extruded Mg-1Al-1Ca-0.2Mn may weaken the texture and suppress twinning initiation, thus alleviating its tension-compression asymmetry [33]. In addition, strain partitioning amongst the variously oriented crystals is also considered a key factor contributing to tension-compression asymmetry in polycrystal Mg alloys, and plays a crucial role in determining yield strength (YS), ductility, and strain hardening behavior, though it remains poorly understood [34]. So far, the mechanism underlying the tension-compression asymmetry in the fine-grained Mg-Mn-Al-Ca-Zn alloy has not been fully understood and warrants further investigation. Moreover, it is also essential to bridge the gap between macroscopic mechanical properties and microscopic deformation mechanisms in these Mg alloys.

In this study, for the first time, we employed in-situ tensile and compressive experiments on the Mg-Mn-Al-Ca-Zn alloy in a synchrotron X-ray diffraction setup. The post-deformed specimens were analyzed using electron backscatter diffraction (EBSD) and transmission electron microscopy (TEM), providing comprehensive insights ranging from microscopic grain structures to macroscopic mechanical responses, offering precise analysis of key factors such as dislocation evolution, twin activation, crystal orientations, and lattice strains.

2. Materials and methods

2.1. Materials

The Mg-0.6Mn-0.5Al-0.5Zn-0.4Ca ingot was prepared by casting (raw materials: pure Mg (99.8 wt.%), pure Al (99.8 wt.%), pure Zn (99.8 wt.%), Mg-20Ca (wt.%) and Mg-3Mn (wt.%) master alloys). The ingot was turned to remove the oxidation surface and processed into a cylindrical ingot with a diameter of Ø80 mm. The ingot was annealed for 8 h at 673 K and cooled in the furnace. Subsequently, hot extrusion was carried out at 673 K with a ram speed of about 0.2 m/min and an extrusion ratio of 25:1. A cylindrical alloy rod with a diameter of 16 mm was obtained for the following experiments.

2.2. In-situ synchrotron X-ray diffraction

The in-situ synchrotron diffraction tension and compression tests of the alloy were carried out at the High Energy Material Science, P07B beamline of the Deutsches Elektronen-Synchrotron (DESY) [35]. Fig. 1 presents the schematic illustration of the experimental setup. The *in-situ* tensile test was conducted at a crosshead speed of 0.3 mm/min. The tensile specimens were machined along with the extrusion direction (ED) of the alloy rod, and cylindrical samples with a gauge length of 25 mm and a diameter of 5 mm were prepared. To maintain an initial strain rate of 2×10^{-4} s^{-1} for both compression and tension, the compression test was performed at a crosshead speed of 0.12 mm/min at room temperature. The compression sample was prepared by machining along the ED of the alloy rod and machining it into a cylinder with a diameter of 5 mm and a length of 10 mm. All tensile, compressive, and EBSD specimens were sampled from the center of the extruded rod. The tensile and compressive tests were each conducted at least five times to ensure the reliability of the results. The reported values represent the average of at least five independent tensile or compressive tests.

A monochromatized synchrotron X-ray beam with an energy of 87 keV, a wavelength of 0.14235 Å, and a beam size of 0.7 × 0.7 mm² was selected for the measurements. The sample-to-detector distance was calibrated by a standard LaB_6 powder sample, and the Perkin Elmer XRD 1622 detector was utilized to collect diffraction patterns. The one-dimensional cake integration of synchrotron X-ray diffraction patterns was performed using Fit 2D software. Subsequently, Gaussian functions were employed to fit the diffraction peaks associated with each crystal plane within the one-dimensional diffraction patterns. For example, Fig. 2(a) illustrates the diffraction pattern of the tensile sample aligned parallel to the loading direction under the unloaded condition. During the tension process, 109 diffraction patterns were recorded to analyze the diffraction peaks evolution of several typical crystal planes. As an example, Fig. 2(b) demonstrates the diffraction peak evolution of $\{11\bar{2}0\}$ plane in Fig. 2(a). It shows that the diffraction peak position gradually shifts to the left (indicating a decrease in the 2θ), while the full

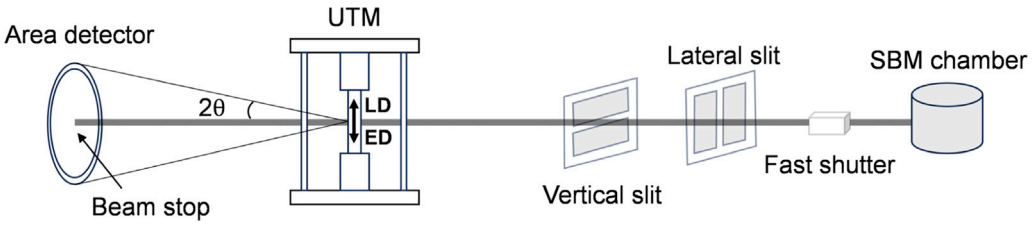

Fig. 1. The schematic of the beamline setup for *in-situ* testing at HEMS P07B, with the mounted UTM positioned on horizontal and vertical linear translation stages. The synchrotron X-ray beam is monochromatized using a single-bounce monochromator, and its size can be adjusted through a collimator. A Perkin Elmer area detector captures diffraction patterns. The loading direction (LD) is parallel to the extrusion direction (ED).

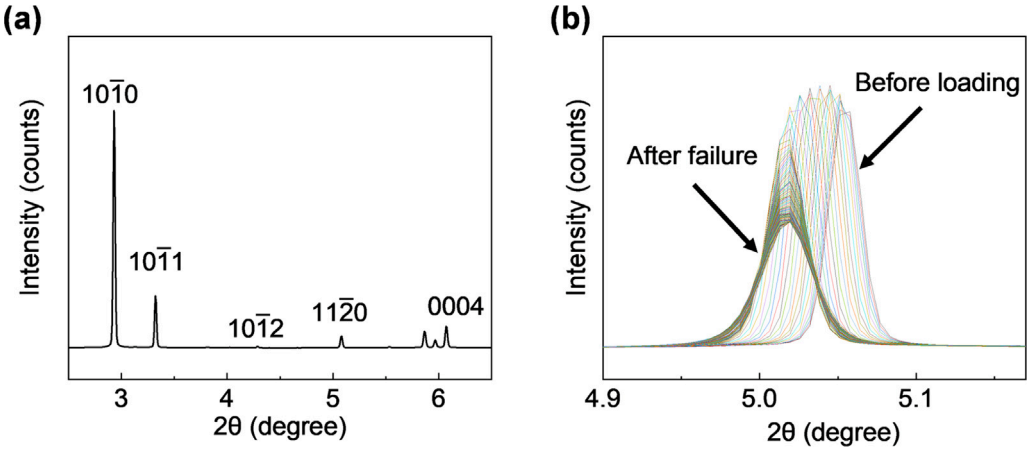

Fig. 2. (a) The X-ray diffraction pattern of the tensile sample in the direction parallel to loading direction. (b) Evolution of diffraction peaks of $\{11\bar{2}0\}$ plane in (a) during the tension process.

width at half maximum (FWHM) increases. Additionally, the diffraction peak intensity initially increases and subsequently decreases.

2.3. Analysis of synchrotron radiation X-ray diffraction data

By analyzing the positions (2θ) of diffraction pattern, the interplanar spacing of the corresponding crystal planes can be determined. Diffraction occurs when the interplanar spacing d_{hkl} of the lattice plane and the angle θ_{hkl} satisfy specific conditions. This condition is described by Bragg's law (Eq. 1):

$$2d_{hkl}sin\theta_{hkl} = \lambda \tag{1}$$

where d_{hkl} is the interplanar spacing of the {hkl} lattice plane, θ_{hkl} represents the diffraction angle of the {hkl} lattice plane, and λ denotes the wavelength. The lattice strain can be calculated by the following formula (Eq. 2) based on the interplanar spacing under different loads:

$$\varepsilon_{hkl} = \left(d_{hkl} - d^i_{hkl}\right)/d^i_{hkl} \tag{2}$$

where d_{hkl} represents the interplanar spacing under different loads, while d^i_{hkl} denotes the initial interplanar spacing.

In general, the FWHM alone is not enough for the calculation of the dislocation density, and the classical Williamson–Hall equation is not valid in the case of dislocations. Thus, the modified Williamson-Hall (MWH) and modified Warren-Averbach (MWA) approaches (Eq. 3) were applied, where the dislocation contrast factors were considered to properly evaluate the dislocation density. These modified approaches have been widely validated and successfully applied in many previous studies, confirming their suitability for the present analysis [36,37]. This dual-method strategy was employed to ensure accurate quantification while accounting for the anisotropic nature of dislocations in hcp Mg. The MWH equation was applied to the XRD data [38,39]:

$$K = \frac{0.9}{L} + \left(\frac{\pi M^2 b^2}{2}\right)^{1/2} \rho^{1/2}\left(K\bar{C}^{1/2}\right) + O\left(K\bar{C}^{1/2}\right) \tag{3}$$

where $K = 1/d$, L represents a grain size, ρ denotes the dislocation density, M represents the dislocation arrangement parameter for weakly correlated dislocations, b denotes the Burgers vector. The average dislocation contrast factors $\bar{C}$ were calculated by the following formula (Eq. 4) [40]:

$$\bar{C} = \bar{C}_{h00}\left(1 - \bar{q}\frac{h^2l^2 + h^2k^2 + l^2k^2}{\left(h^2 + k^2 + l^2\right)}\right) \tag{4}$$

where $\bar{C}_{h00}$ is the average contrast factor and $\bar{q}$ is dependent on the dislocation type obtained using the ANIZC software. For enhanced accuracy, the MWA method was subsequently employed. The Fourier coefficients of the diffraction peaks were analyzed using [41]:

$$lnA(L) = lnA^S(L) - \rho\frac{\pi b^2 L^2}{2}\ln\left(\frac{R_e}{L}\right)\left(K^2\bar{C}\right) + o\left(K^4\bar{C}^2\right) \tag{5}$$

where L represents the Fourier length, $A^S(L)$ represents the size Fourier coefficients and R_e represents the effective outer cut-off radius. The dislocation density ρ and the effective

outer cut-off radius R_e were obtained by fitting the $lnA(L)$ vs. L^2curve. The parameter $M = R_e\sqrt{\rho}$ was then calculated and fed back into the MWH method for optimization.

2.4. Microstructural characterization

The microstructure was analyzed using EBSD on a JEOL JSM-7800F SEM with a step size of 0.2 μm. EBSD specimens were first ground with sandpaper and then mechanically polished using a 0.5 μm diamond spray polishing suspension. Subsequently, the electropolishing was carried out at 253 K using a solution containing 5% perchloric acid and 95% ethanol for 30 s with a voltage of 20 V. The microstructure of the alloy was further analyzed using a Talos F200S TEM. The preparation of TEM samples involved the following steps. First, a 0.5 mm-thick slice was wire-cut from the alloy and gradually ground to 50 μm using sandpaper. Next, the sample was thinned using a Gatan PIPS691 argon ion milling instrument. The ion milling process started at 4.2 kV and 5°, then continued at 2 kV and 2° for 30 min after hole appeared.

3. Results

3.1. Microstructure of extruded alloy

Fig. 3 illustrates the microstructure of the extruded Mg alloy. The inverse pole figure with respect to the sample X-direction (IPF-X) in Fig. 3(a) shows the incomplete dynamic recrystallization occurred in the Mg alloy matrix. The microstructure consists of uncrystallization regions aligned along the ED and uniformly distributed fine equiaxed recrystallized grains. Previous studies identified the presence of Al_8Mn_5 and $(Mg, Al)_2Ca$ particles in the alloy [42]. After extrusion, their fragmentation and uniform dispersion enhanced recrystallization nucleation and inhibited grain growth, resulting in a refined grain structure [43]. A grain size distribution map for the recrystallized grains was generated by analyzing EBSD data, excluding grains smaller than 0.5 μm. The extruded alloy exhibited an average recrystallized grain size of 1.73 μm (Fig. 3(b)). The pole figure reveals a maximum texture intensity of 10.82 (Fig. 3(c)). The small equiaxed recrystallized grains in the IPF exhibit relatively random orientations, with $\langle 10\bar{1}0\rangle$ or $\langle 11\bar{2}0\rangle$ directions of most grains aligned parallel to the ED. In contrast, coarse grains refer to incompletely recrystallized grains that are larger than the fully recrystallized fine grains and distinct from uncrystallized regions. EBSD analysis (Fig. 3c) shows that these coarse grains exhibit a strong extrusion fiber texture with the $\langle 10\bar{1}0\rangle$ orientation parallel to the ED, which contributes to the maximum texture intensity observed in the pole figure. Quantitative analysis using Image Pro software revealed that the recrystallized area fraction is 84.2%, with the remainder consisting of such coarse grains. These grains may not suppress twinning as effectively as fine recrystallized grains, particularly under compression, where twinning is more easily activated. Fig. 3(d) presents

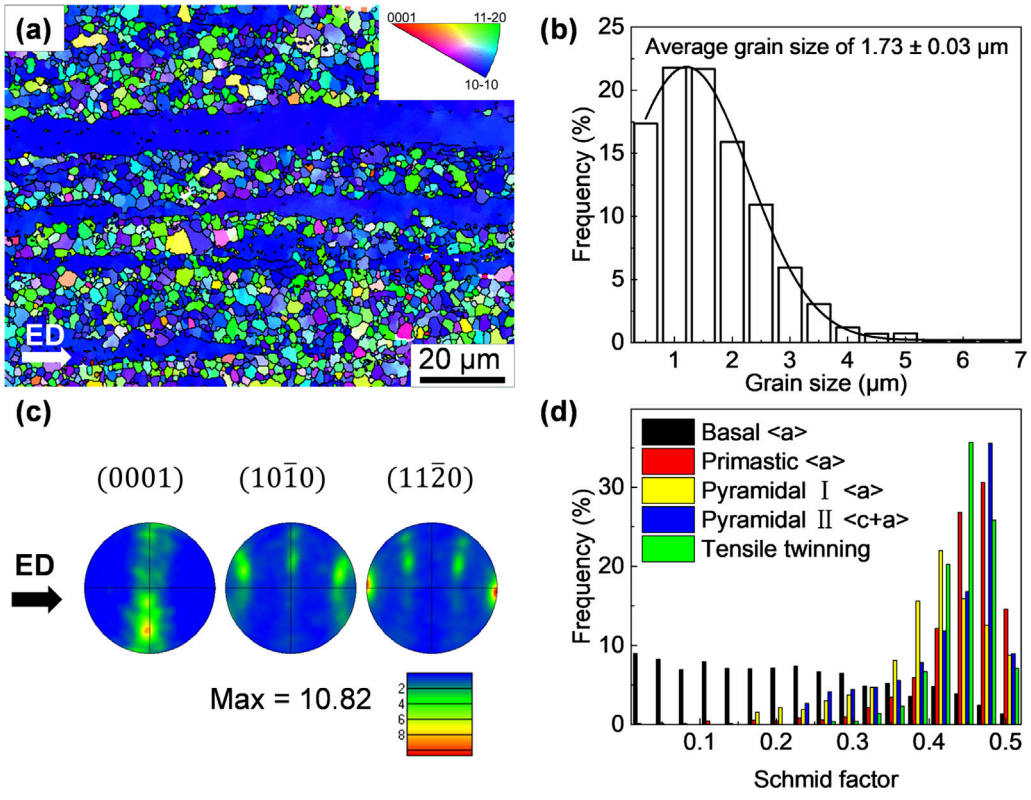

Fig. 3. Microstructures of the extruded alloy: (a) IPF-X map showing a bimodal microstructure; (b) grain size distribution; (c) pole figures with a maximum intensity of 10.82; (d) the distribution diagram of the Schmid factors.

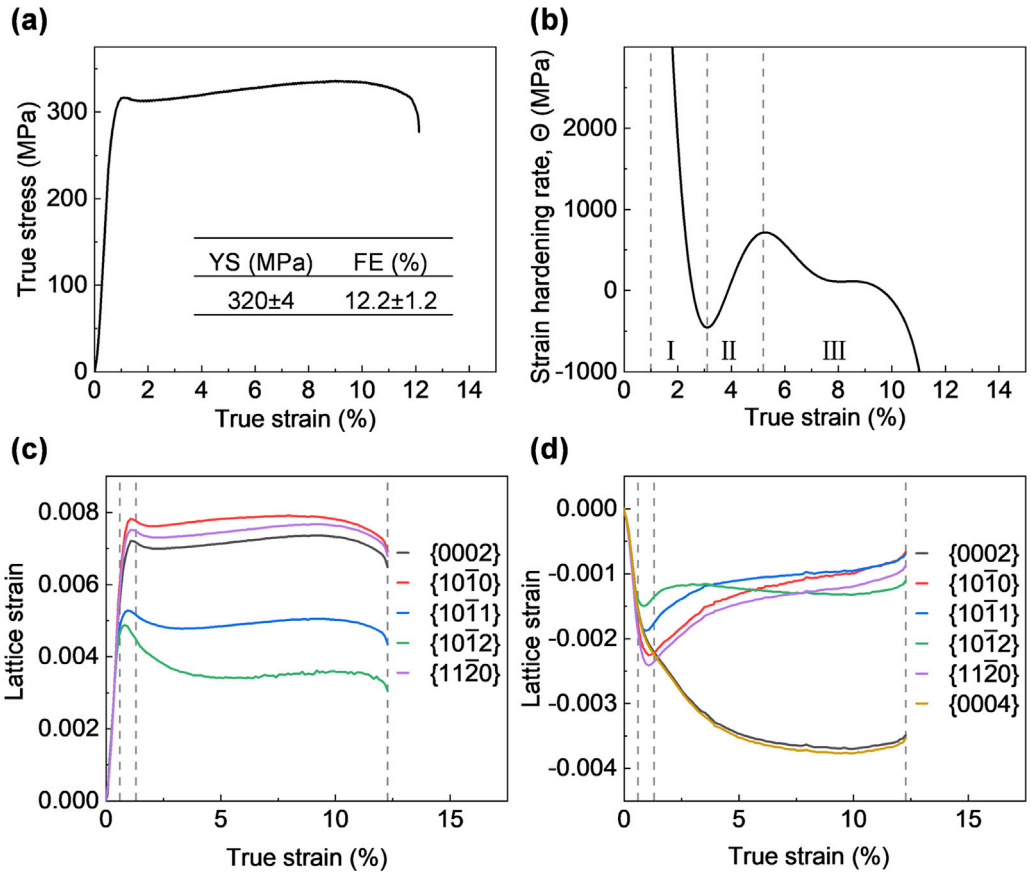

Fig. 4. (a) Representative room temperature tensile true stress-strain curve of extruded Mg-0.6Mn-0.5Al-0.5Zn-0.4Ca alloys. (b) Strain hardening rate curve obtained during compression. (c) Lattice strains planes parallel to the tensile direction. (d) Lattice strains perpendicular to the tensile direction. The evolution of lattice strains can be divided into three regions.

the Schmid factor distribution for various deformation modes in the extruded alloy. Basal ⟨a⟩ slip has lower Schmid factors than nonbasal ⟨a⟩ and ⟨c + a⟩ slips, making the latter easy to activate. In addition, the high Schmid factor of tensile twinning indicates it is likely to be activated during deformation.

3.2. In-situ tension of the extruded Mg alloy

The in-situ tensile stress-strain curve at room temperature of the studied alloy is shown in Fig. 4(a). The extruded alloy exhibits a tensile yield strength of 320 MPa, a ultimate tensile strength (UTS) of 324 MPa, and a fracture elongation (FE) of 12.2%. The alloy yields at a strain of 1.2%, marking the transition from the elastic deformation stage (strain: 0 ∼ 1.2%) to the plastic deformation stage (strain: 1.2 ∼ 12.2%). Interestingly, the alloy did not exhibit apparent strain hardening following yielding. In fine-grained Mg alloys, limited dislocation interactions weaken strengthening, and twinning is restricted, thereby reducing its strain-hardening rate (SHR). The SHR curve can be divided into three distinct stages (Fig. 4(b)). The first stage, known as the elastic-plastic transition, marks a sharp decrease in SHR and signifies the onset of plastic strain. In the second stage, SHR increases slightly until the strain rate reaches 5.2%. Finally, in the third stage, SHR gradually decreases.

Fig. 4(c and d) shows the lattice strains evolutions parallel and perpendicular to the tensile direction. Fig. 4(c) shows the lattice strains parallel to the tensile direction exhibit an increasing trend. Based on lattice strain evolution, the curve can be divided into three distinct regions: the elastic deformation region (Region I), the elastic-plastic deformation region (yield region, Region II), and the plastic deformation region (Region III). In Region I, the lattice strain of each plane increases linearly with the strain. The nearly identical slopes of the curves for each plane indicate that their Young's moduli are approximately equal. At the start of Region II, the lattice strains begin to deviate from linearity, indicating the onset of grain yielding. The lattice strains of the {10$\bar{1}$1} and {10$\bar{1}$2} planes deviate from linearity earlier, suggesting that these planes are more prone to premature yielding and carry a lower load. In contrast, the {0002}, {11$\bar{2}$0} and {10$\bar{1}$0} planes yield simultaneously during the yielding process, carrying a higher load. The {10$\bar{1}$0} planes exhibit the highest lattice strains and carry the maximum load during deformation. At the initial stage of Region III, the lattice strains begin to decrease and then stabilize as the strain increases. Just before fracture, the lattice strains of all crystal planes decrease with strain, indicating that all lattice planes experience compressive stress due to contraction from elastic deformation.

The lattice strains perpendicular to the loading direction show a decreasing trend during tension due to the compressive stress (Fig. 4(d)). The evolution of lattice strains can similarly be divided into three regions. Differently, upon yielding, the lattice strains of the $\{10\bar{1}1\}$ and $\{10\bar{1}2\}$ planes are lower, whereas the lattice strains of the {0002} plane is the highest. In general, the CRSS for basal slip in Mg alloys is the lowest, making it the first slip system to be activated under stress [44]. As a result, the {0002} plane is expected to carry the least load during deformation. Notably, in this study, the {0002} plane carries higher loads on both the crystal planes parallel and perpendicular to the loading direction. This atypical load distribution is primarily attributed to the preferred orientation of grains [45]. The studied alloy exhibits a pronounced texture, with the $\{10\bar{1}0\}$ and $\{11\bar{2}0\}$ planes of most grains oriented perpendicular to the ED. Among the planes perpendicular to the loading direction, the $\{10\bar{1}0\}$ and $\{11\bar{2}0\}$ planes carry the highest load. Meanwhile, in the planes parallel to the tensile direction, the {0002} planes are predominant, resulting in the {0002} planes carrying the highest load. In addition, although the CRSS for basal ⟨a⟩ slip is the lowest among all slip systems in Mg alloys, the activation of basal slip is also influenced by its Schmid factor. In this study, the basal ⟨a⟩ slip system has a low Schmid factor (Fig. 3(d)), resulting in reduced resolved shear stress. Consequently, basal slip is not readily activated during the early deformation stages, allowing {0002} planes to carry higher elastic stresses compared to more favorably oriented non-basal systems.

Fig. 5(a) shows the evolution of the FWHM of the XRD peaks with the increase of strain during tension. In the elastic region, the FWHM of almost all peaks decreases slightly with increasing strain. After yielding, the FWHM of all peaks increases rapidly. This shows fast defect generation or dislocation multiplication. As strain increases, the growth rate slows down. Near fracture, the FWHM of all peaks becomes almost constant. Fig. 5(b) shows the evolution of dislocation density during tension. The initial dislocation density of the extruded alloy is 5.04×10^{14} m^{-2}. In Region I (strain of 0 ~ 0.35%), the dislocation density gradually decreases with increasing true strain. The observed reduction in dislocation density in Region I can be explained by two complementary processes. First, short-range annihilation of opposite-sign dislocations can occur when mobile dislocations glide and annihilate each other, reducing the net Burgers vector content [46,47]. Second, reorganization/recovery of the initial dislocation network may take place. Under low applied stresses, dislocations can rearrange into more correlated, low-energy configurations such as dislocation walls, subgrain boundaries, or cells. Such rearrangement does not necessarily remove dislocations, but it increases their spatial correlation and reduces the XRD peak broadening attributed to random dislocations. As a result, XRD analysis may report an apparent decrease in dislocation density even though a large population of dislocations remains [48,49]. Because the initial extruded alloy is only partially recrystallized (recrystallized fraction = 84.2%), the dislocation distribution is heterogeneous, which may further enhance such effects. With increasing tensile stress, the resolved shear stress surpasses the CRSS of specific slip systems, activating additional dislocation slip. However, due to the pinning effect of the Cottrell atmosphere, the movement of dislocations is hindered, resulting in slow dislocation movement. Therefore, the dislocation density increases slowly in this region. Once a balance is established between dislocation annihilation and multiplication, the dislocation density in the alloy temporarily stabilizes. In the yield region (Region II, strain of 0.35 ~ 1.3%), the applied stress becomes sufficiently high for dislocations to overcome their constraints and move rapidly. At this stage, more slip systems are activated as the resolved shear stress exceeds their CRSS, rapidly increasing dislocation density. Notably, the dislocation density begins to increase rapidly at a strain of 0.35%, before the yield point (strain of 1.3%). It is attributed to certain planes, such as $\{10\bar{1}1\}$, $\{10\bar{1}2\}$, and $\{10\bar{1}3\}$, begin to yield at this stage, indicating the initiation of dislocations. In Region III, the generation of new dislocations slows down while existing

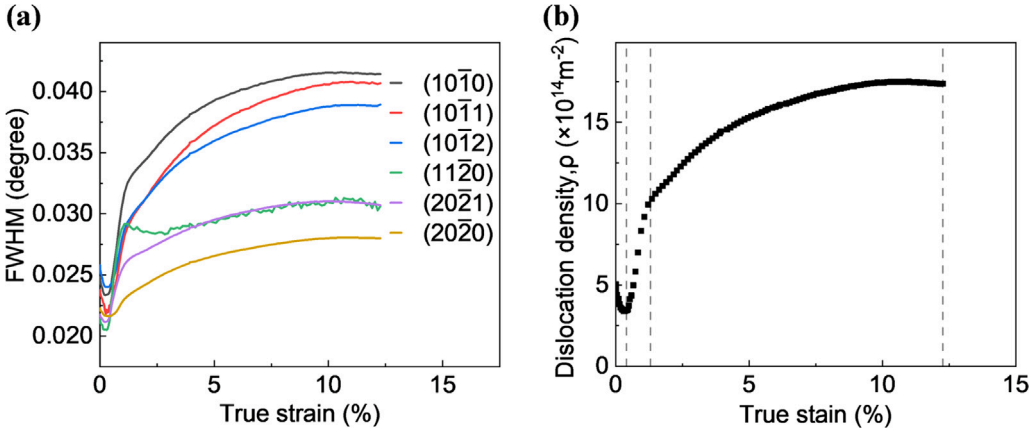

Fig. 5. (a) Evolution of FWHM of the XRD peaks with the increase of strain during tension. (b) Evolution of dislocation density with true strain. Dislocation density evolves through three stages: Region I (where dislocation annihilation dominates), Region II (yield region, where rapid dislocation multiplication occurs), and Region III (dislocation proliferation slows and reaches maximum density).

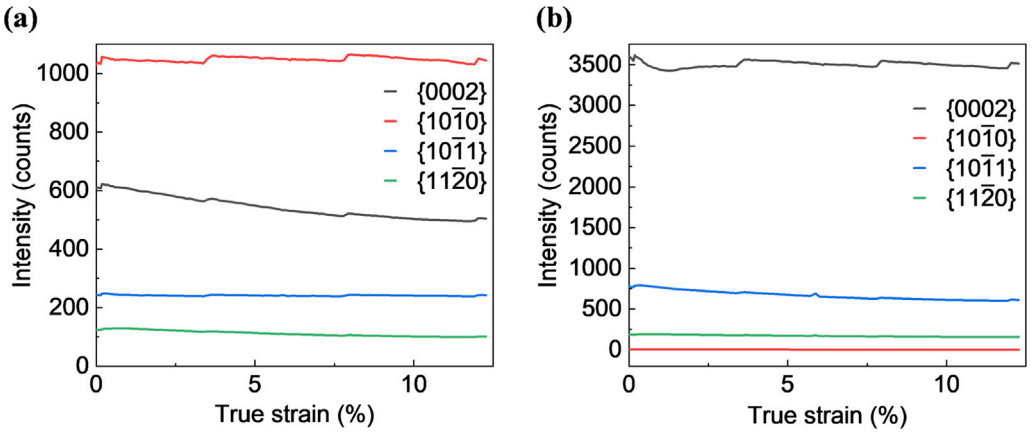

Fig. 6. (a) Evolution of diffraction intensity parallel to the tensile direction. (b) Evolution of diffraction intensity perpendicular to the tensile direction. Diffraction intensity stays stable, showing little grain orientation change.

dislocations gradually proliferate until reaching their maximum density.

Fig. 6 shows the diffraction intensity evolution of each plane. Before loading, the extruded alloy exhibits a fiber texture characterized by most grains with the ⟨10$\bar{1}$0⟩ parallel to the ED and some with the ⟨0002⟩ parallel to the ED. These observations align with the EBSD results presented in Fig. 3(d). Fig. 6 also demonstrates that the diffraction intensity of all planes does not change significantly throughout the whole tension process, indicating minimal variation in the grain orientation of the alloy during deformation.

To further study the tensile deformation mechanism, the microstructure of the extruded alloy after 10% tensile strain was characterized using EBSD (Fig. 7). The BC map reveals that few twins form during deformation. Combined with the synchrotron X-ray diffraction results, the lattice strain of the {10$\bar{1}$2} plane deviates from linearity before yielding, indicating easier yielding and the lower load carried during tension. This suggests that tensile twins are more readily activated during deformation. Previous studies indicate that tensile twins tend to form in deformed Mg alloys due to their low CRSS [50]. However, this is somewhat different from the EBSD observation results. This is primarily attributed to the influence of texture, which subjects the C-axis of most grains to compressive stress. The high CRSS needed for compression twins makes their activation challenging [51]. Only a limited number of grains experience tensile stress along the C-axis, forming tensile twins in a few grains. Furthermore, the fine grain of the alloy also inhibits the activation of twins to a certain degree, contributing to this behavior. Fig. 7(d) illustrates the distribution of Schmid factors for the tensile sample. Texture results in low Schmid factors for basal slip, mostly below 0.3, while non-basal ⟨a⟩ and ⟨c + a⟩ slips show values mainly above 0.3.

Fig. 8 presents the TEM images of the extruded alloy after 10% tensile deformation. Owing to the fine grain size and high CRSS for twinning, dislocation slip serves as the main deformation mechanism in the alloy. The TEM image of the large grain interior reveals some dislocations (Fig. 8(a)). Using the "$\boldsymbol{g}\cdot\boldsymbol{b} = 0$ is invisible" criterion, dislocation types were identified through two-beam diffraction. Under $\boldsymbol{g} = 0002$, a significant number of dislocations are visible, implying they are either ⟨c⟩ dislocations or ⟨c + a⟩ dislocations containing ⟨c⟩ components, as indicated by the red and yellow arrows in Fig. 8(c). Some of these dislocations were also observed under $\boldsymbol{g} = 01\bar{1}0$, as shown by the red arrows in Fig. 8(d), confirming that they are ⟨c + a⟩ dislocations because ⟨c⟩ dislocations are extinguished under this condition. Conversely, the dislocations highlighted by the yellow arrows in Fig. 8(c) are absent in Fig. 8(d), indicating they are ⟨c⟩ dislocations. It demonstrates that the activation of ⟨c⟩ and ⟨c + a⟩ dislocations is a crucial deformation mechanism in the alloy. A few ⟨a⟩ dislocations, which remain visible under $g = 01\bar{1}0$, are also observed in Fig. 8(b). Additionally, the TEM image of the fine-grain interior reveals a higher density of dislocations (Fig. 8(e)). Many dislocations can still be seen under $g = 0002$ (Fig. 8(f)), suggesting activation of ⟨c⟩ or ⟨c + a⟩ dislocations. Dense dislocation tangles were observed in both coarse and fine grains after deformation, which is consistent with the increased dislocation densities obtained from the MWH/MWA analysis.

3.3. In-situ compression of extruded alloy

Fig. 9(a) shows the room-temperature compressive stress-strain curve of the extruded alloy. The compressive yield strength of the extruded alloy is 236 MPa, while the ultimate compressive strength reaches 432 MPa, with an FE of 11.3%. The alloy behaves differently under tension and compression, indicating asymmetry. Fig. 9(b) shows that the SHR curve during compression can also be divided into three stages, like those observed in the tension process.

The lattice strains evolution of crystal planes during compression was determined by analyzing the plane spacing measured under different strain levels, as illustrated in Fig. 9(c and d). Crystal planes perpendicular to the loading direction experienced compressive stress, resulting in a decreasing trend in interplanar spacing. The lattice strains evolution can similarly

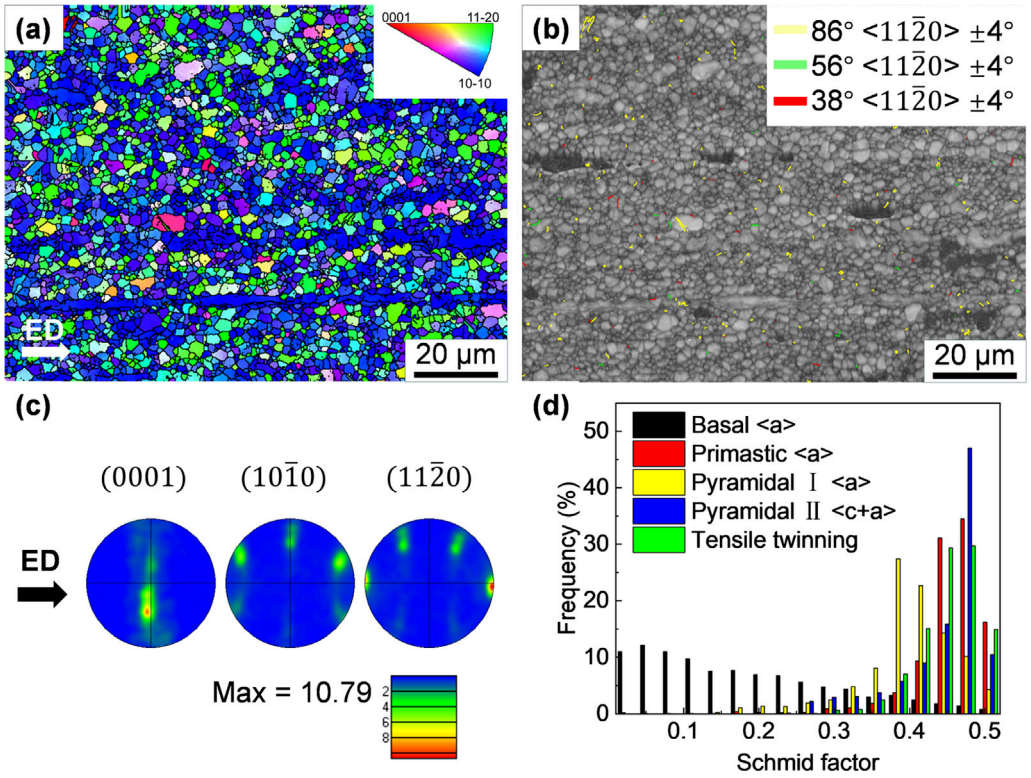

Fig. 7. EBSD results of the extruded alloy with a tensile deformation strain of 10%: (a) IPF-X map; (b) BC map indicating limited twin formation; (c) pole figures with a maximum intensity of 10.79; (d) the distribution diagram of the Schmid factors.

be segmented into those three regions. In Region I (elastic region), the lattice strains of most planes increase linearly with the strain, and the slopes are consistent. Notably, the interplanar spacings of the {0002} planes remain nearly unchanged, indicating that these crystal planes exhibit minimal lattice strains. It is primarily attributed to the strong fiber texture of the extruded alloy, where most {0002} are aligned with the loading direction, and few are oriented perpendicularly. At the start of Region II, crystal planes begin to yield, and their lattice strains are significantly lower than those at the tensile yield point. For instance, the {10$\bar{1}$0} planes yield at a strain of about 0.002, compared to 0.0076 in tension (Fig. 4(c)). In Region III (plastic deformation region), the lattice strains of crystal planes (other than {0002}) continue to increase at a nearly constant rate with increasing strain, and this trend persists until final fracture. Notably, after yielding, the lattice strains of the {0002} gradually increases, eventually reaching the maximum and carrying the highest load. This phenomenon will be further explored in Section 4.1.1. Crystal planes parallel to the loading direction experienced tensile stress, resulting in an increasing trend in interplanar spacing. In Region I (elastic region), the lattice strains of most crystal planes increase linearly with the strain, showing a uniform slope. The {0002} plane deviates from linearity before yielding due to its low CRSS, which facilitates basal slip under tensile stress. In Region II (elastoplastic region), lattice strain deviates from linearity for all planes, with the {10$\bar{1}$0} planes yielding earlier, followed by the {10$\bar{1}$2} and {10$\bar{1}$1} planes. In Region III (plastic deformation region), the {10$\bar{1}$0}, and {10$\bar{1}$2} planes exhibit higher lattice strain, indicating they carry the highest load during deformation.

Fig. 10(a) shows the evolution of the FWHM of the XRD peaks with increasing compression strain. Fig. 10(b) shows the evolution of dislocation density during compression. The initial dislocation density of the compression specimen is 5.19×10^{14} m^{-2}, comparable to that of the tensile specimen. The dislocation density evolution during compression closely mirrors that observed in tension. Initially, there is a slight decrease in dislocation density (Region I), followed by a rapid increase after yielding (Region II), and then it stabilizes gradually (Region III). However, when approaching failure, the dislocation density of the alloy increases rapidly again (Region IV). It can be attributed to local stress concentrations that develop during late-stage compression. Such stress concentrations commonly arise from intensive twin nucleation/growth, twin–twin and twin–grain boundary interactions, and the formation of localized deformation bands (micro-shear bands), all of which promote enhanced dislocation nucleation and multiplication locally. Previous experimental and review studies have documented these processes in Mg and other hexagonal metals: twins generate strong local stress fields and interact with lattice dislocations, promoting dislocation emission and pile-up at twin tips and twin boundaries; these interactions in turn can nucleate localized shear bands and localized high dislocation density regions that give rise to the observed rapid increase in bulk dislocation content [52,53].

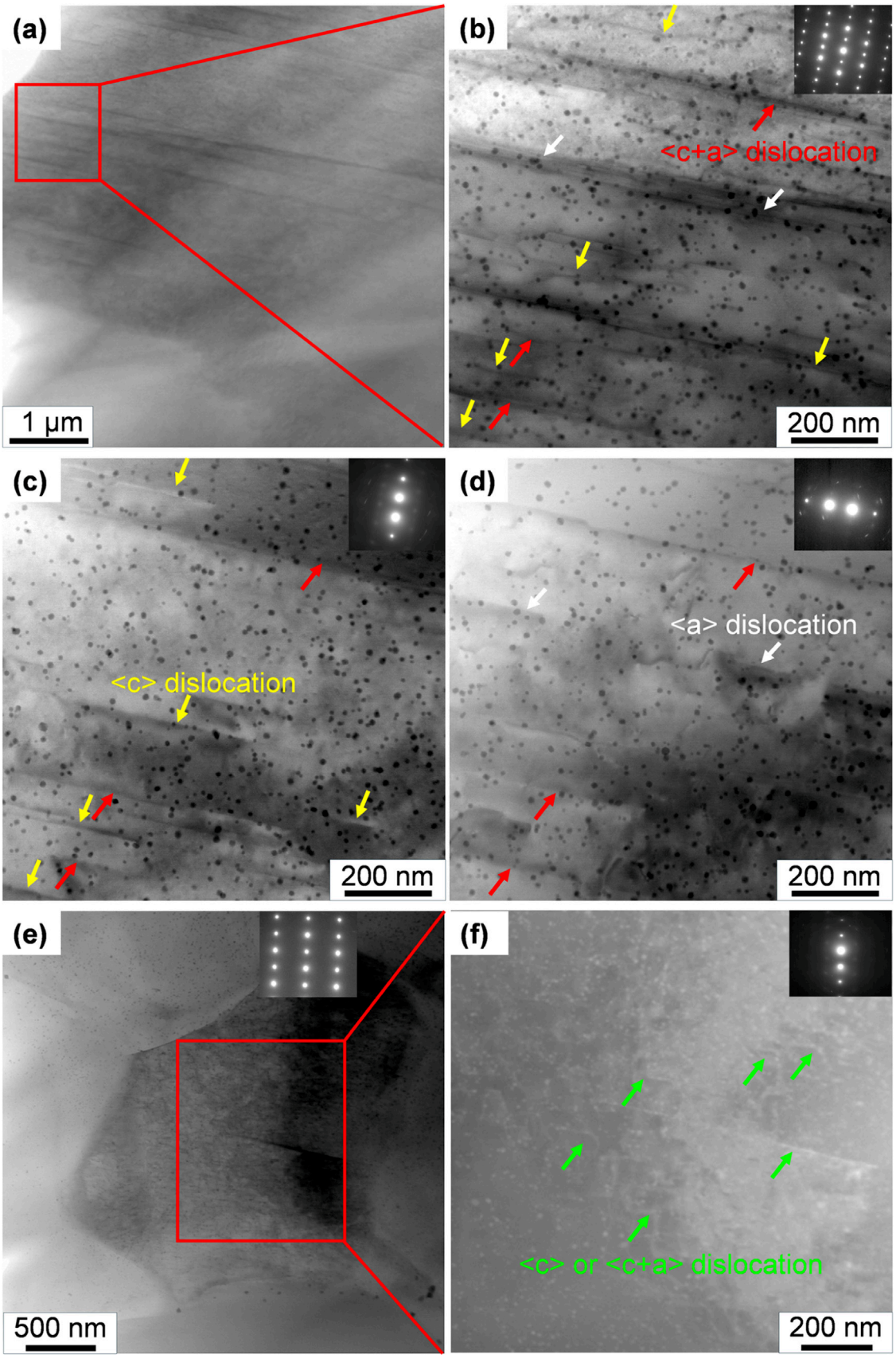

Fig. 8. Bright-field TEM image of the extruded alloy with a tensile strain of 10%: (a) Bright-field TEM image of a large grain; (b) same grain viewed along the $\langle 11\bar{2}0\rangle$ zone axis; (c) two-beam image of the large grain with $g = 0002$; (d) two-beam image of the large grain with $g = 01\bar{1}0$; (e) fine grain imaged along the $\langle 11\bar{2}0\rangle$ zone axis; (f) two-beam image of the fine grain with $g = 0002$.

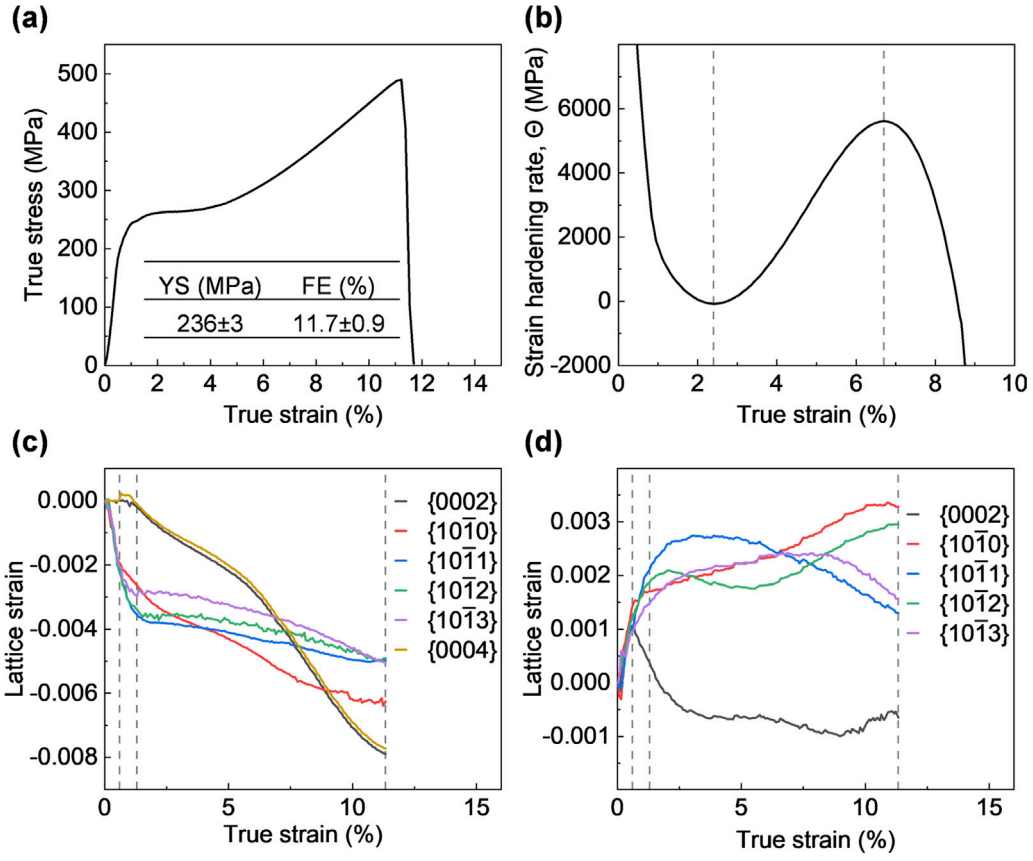

Fig. 9. (a) Representative room temperature compressive true stress-strain curve of extruded alloy. (b) Strain hardening rate curve obtained during compression. (c) Lattice strains parallel to the compression direction. (d) Lattice strains perpendicular to the compression direction. The lattice strains evolution can be divided into Region I (elastic region), Region II (the elastic-plastic region), and Region III (plastic deformation region).

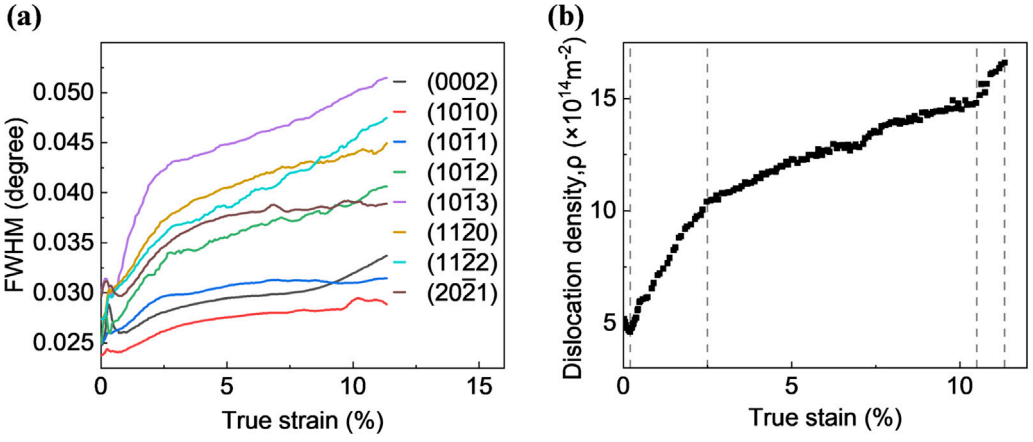

Fig. 10. (a) Evolution of FWHM of the XRD peaks with the increase of strain during compression. (b) Dislocation density evolution with strain. The dislocation density evolution can be divided into Region I (elastic region, with a slight decrease in dislocation density), Region II (a rapid increase after yielding), Region III (plastic deformation region, where it gradually stabilizes), and Region IV (failure region, with a rapid increase before failure).

Fig. 11 shows the diffraction intensity evolution of each crystal plane. Before the start of compression loading, the extruded alloy exhibits a fiber texture, characterized by a large number of grains with ⟨10$\bar{1}$0⟩ parallel to the ED, and some with ⟨0002⟩ perpendicular to the ED. In Region I (strain: 0 ∼ 0.7%), the diffraction intensity of the crystal planes remains almost unchanged in both the parallel and perpendicular directions relative to the loading direction. The alloy is still elastically deforming, and stress and strain distribute uniformly. Grain boundary movement is restricted, limiting changes in grain orientation and texture. When the strain exceeds 0.7%, the diffraction intensity of the {0002} plane begins to in-

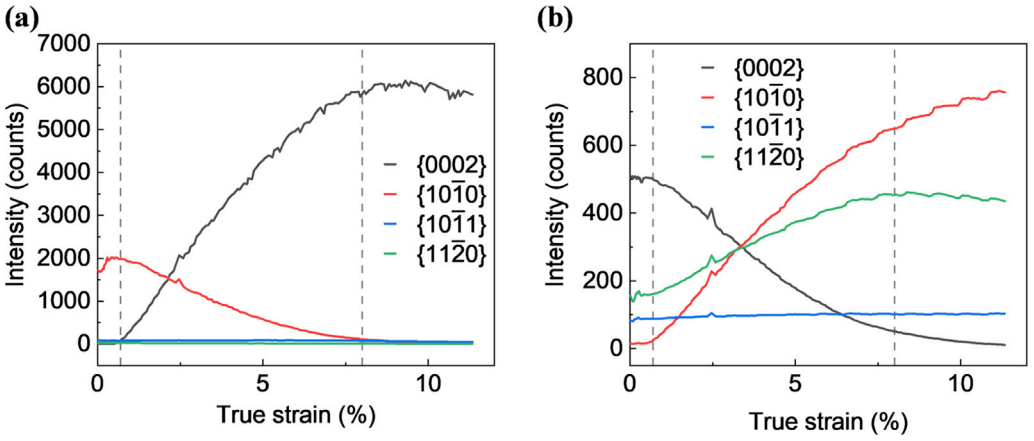

Fig. 11. (a) Evolution of diffraction intensity parallel to the compression direction. (b) Evolution of diffraction intensity perpendicular to the compression direction. The evolution of grain orientation can be divided into Region I (elastic region, with stable diffraction intensity), Region II (elastic-plastic transition region, where grain orientation shifts rapidly), and Region III (plastic deformation region, where orientation stabilizes).

crease rapidly along the loading direction, while that of the {10$\bar{1}$0} plane decreases. Conversely, in the direction perpendicular to the loading direction, the diffraction intensity of the {0002} plane rapidly decreases, while that of the {10$\bar{1}$0} and {11$\bar{2}$0} planes increase. These changes indicate a rapid shift in the grain orientation of the alloy. In Region III (strain: 8 $\sim$ 11.3%), the diffraction intensity of each plane in both directions shows little variation, indicating that the grain orientation is largely stabilized. As the strain increases, plastic deformation within the grains continues to accumulate until it reaches a state of strain saturation. Once saturation is achieved, the deformation within the grains stabilizes, resulting in the stabilization of grain orientation.

Fig. 12 presents the EBSD characterization of the alloy after compression. Fig. 12(b) shows numerous tension twins in the compressed alloy. Such twins can cause grain rotations of 86°, leading to significant changes in the orientation of grains [54]. Initially, most grains have their c-axes perpendicular to the loading direction. After undergoing a rotation of 86°, their c-axes align nearly parallel to the loading direction. This phenomenon is illustrated in Fig. 12(a and c), where the IPF map and pole figures show that the c-axes of most grains align with the loading direction. The maximum texture intensity of the compressed alloy reaches 52.61, indicating the development of a strong texture. Fig. 12(d) illustrates that basal ⟨a⟩ slip has a higher Schmid factor in the compressed sample compared to the tensile one. The difference in the Schmid factor between the compression and tension samples is primarily due to changes in the grain orientation during compression. The Schmid factors for non-basal and ⟨c + a⟩ slips are primarily distributed within the range greater than 0.2, showing negligible differences compared to the tensile sample. In contrast, after compression, grain rotation and texture evolution lead to many grains aligning their c-axes with the tensile direction, significantly increasing the resolved shear stress and Schmid factor of {10$\bar{1}$2} twinning.

4. Discussion

4.1. Deformation mechanisms

4.1.1. Evolution of lattice strains

The evolution of lattice strains in different crystal planes during deformation is influenced by the initial texture. During tensile deformation, the grain orientation remains nearly unchanged, resulting in a stable texture. This stability ensures a consistent and predictable evolution of lattice strains. In general, basal ⟨a⟩ slip in Mg alloys has the lowest CRSS and is expected to be activated first, which would normally result in the {0002} planes carrying the least load during deformation. However, the studied alloy exhibits a strong texture that markedly reduces the Schmid factor of the basal ⟨a⟩ slip system (Fig. 3(d)), thereby suppressing its activation in the early stages of straining. As a result, the {0002} planes are unable to effectively release the applied stress through basal slip and instead sustain relatively high elastic stresses. This atypical stress partitioning indirectly facilitates the activation of non-basal slip systems, which play a more significant role in accommodating plastic deformation. Thus, the higher load observed on the {0002} planes is not a direct indication of basal slip activity, but rather a consequence of texture-induced suppression of basal slip and the associated promotion of non-basal slip. During compressive deformation, the evolution of lattice strains exhibits interesting phenomena due to changes in texture. Notably, after yielding, the ⟨0002⟩ lattice strain along the loading direction increases gradually, indicating that it carries an increasing load. As shown in Fig. 11, it is primarily attributed to changes in grain orientation after yielding. Specifically, the {0002} planes of most grains gradually shift from parallel to the loading direction to perpendicular. Consequently, the {0002} planes eventually exhibit the largest lattice strains and carry the highest load.

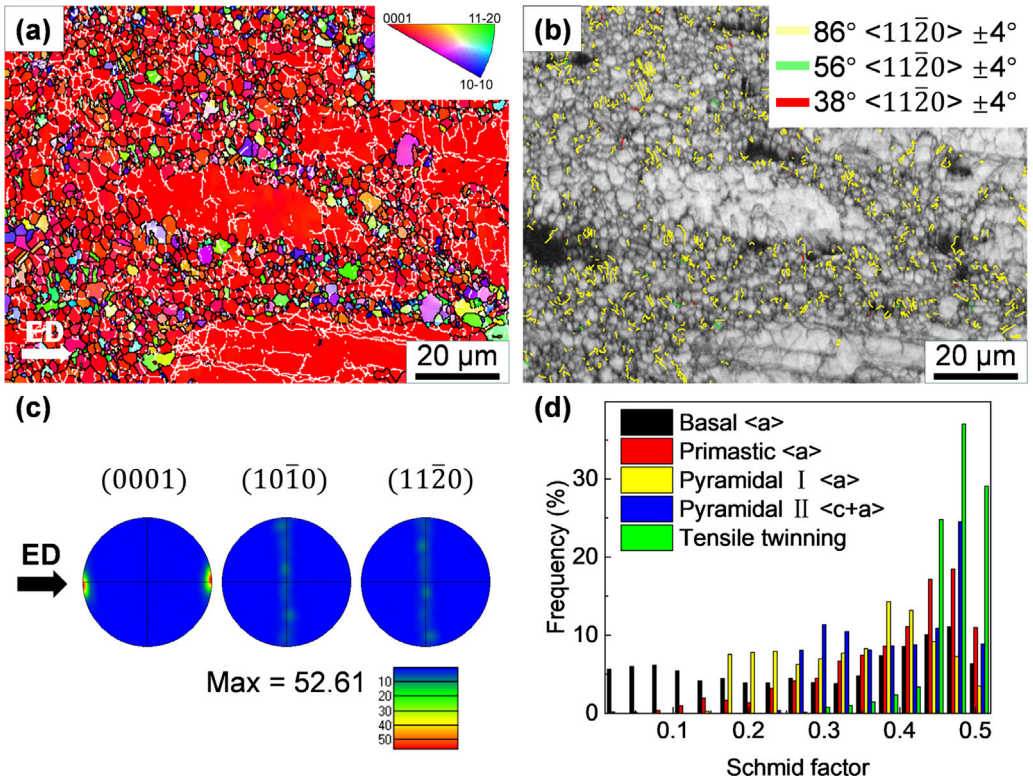

Fig. 12. EBSD results of the extruded alloy after compression: (a) IPF-X map; (b) BC maps extensive tensile twinning; (c) pole figures with a maximum intensity of 52.61; (d) the distribution diagram of the Schmid factors.

4.1.2. Dislocation slips versus *deformation twinning*

In-situ synchrotron X-ray diffraction results (Fig. 5 and Fig. 10) reveal a significant activation and continuous proliferation of dislocations during both tension and compression processes. From the TEM results (Fig. 8), not only are ⟨a⟩ dislocations activated, but ⟨c⟩ and ⟨c + a⟩ dislocations also play a significant role during tension. In addition, more dislocations are activated inside the fine grain, resulting in a higher dislocation density. Previous research has shown that in fine-grained materials, ⟨c⟩ and ⟨c + a⟩ slip mechanisms are more readily activated to accommodate deformation, whereas larger grains tend to rely on twinning for deformation adaptation [55]. When the grain size is smaller than about 5.5 μm, twinning activation is suppressed, making it easier to observe a higher level of dislocation activity in fine grains [56]. The finer grain and texture of the studied alloy hinder the initiation of basal slip and tension twins, which have lower CRSS. Instead, it necessitates the activation of non-basal ⟨a⟩ slip and ⟨c + a⟩ slip with higher CRSS, making dislocations more likely to dominate the deformation. The activation of these dislocation slips, especially ⟨c + a⟩ dislocations, facilitates crystal slip and plastic deformation, significantly improving the plastic deformation capability and its ductility [57,58].

After yielding during compression, the grain orientation of the alloy undergoes significant changes, which confirms the extensive activation of tensile twinning. EBSD results of compressed alloy also show the initiation of tensile twins leads to changes in grain orientation and the development of a strong compression texture (Fig. 12(c)). In AM magnesium alloys, texture evolution during deformation can arise from low angle grain rotations due to dislocation accumulation or from twin formation. However, as shown in Fig. 6, the diffraction intensity of planes remains almost unchanged during room-temperature tension. Similarly, Fig. 3(c) and Fig. 7(c) show that the overall texture intensity changes little after tensile deformation. As a result, the possibility of texture evolution caused by grain rotation or low-angle boundary formation during room-temperature deformation is minimal. Therefore, the texture evolution during room-temperature deformation is mainly caused by twin formation. Accordingly, the increase in diffraction peak area can be attributed to the formation of new twins, and estimating the twin volume fraction from XRD peak area is justified. Fig. 13 shows the variation in {10$\bar{1}$2} tension twin volume fraction during compression. This fraction was estimated by dividing the increase in the area of the ⟨10$\bar{1}$0⟩ peak by the area of all peaks [59]. This approach is well established and reliable, as the formation of {10$\bar{1}$2} tensile twins rotate the c-axis by ∼86°, producing a measurable and systematic increase in the intensity of the ⟨10$\bar{1}$0⟩ peak. The peak areas were integrated over a small azimuthal range (near the peak apex), which approximates the peak height. Although this may slightly underestimate the absolute twin volume fraction, it ensures a consistent and reproducible trend with strain. Importantly, this method does not assume that all grains rotate into an identical orientation after twinning. Instead, it captures the relative intensity change as-

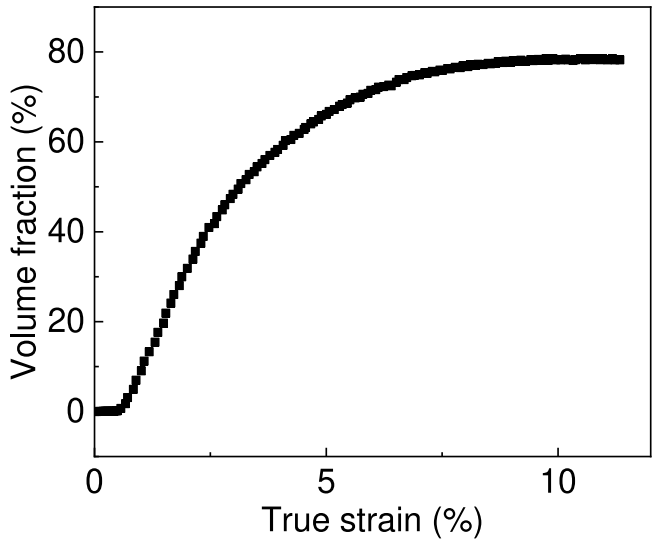

Fig. 13. The volume fraction of $\{10\bar{1}2\}$ twins as a function of true strain during compression.

sociated with twin-related reflections, which reliably reflects the extent of twinning. While possible sources of error include peak overlap, incomplete detection of all twin variants, and heterogeneity in grain orientation, these factors mainly affect the absolute value rather than the observed trend. Therefore, the calculated twin volume fraction provides a robust and reliable measure of the evolution of twinning with strain. The volume fraction of the tension twin increases rapidly following the onset of yielding and then gradually stabilizes as deformation progresses. It indicates that tension twins dominate the grain deformation at the onset of plastic deformation during compression. Although twinning dominates at this stage, it does not suppress dislocation activity; instead, it promotes dislocation generation and accumulation through multiple mechanisms such as stress concentration, slip activation, and dislocation–twin interactions [60], leading to a rapid increase in dislocation density. Compared to tensile sample, compressed sample exhibits a higher Schmid factor for basal ⟨a⟩ slip, indicating easier activation during compression. The high Schmid factors for non-basal ⟨a⟩ slip and ⟨c + a⟩ slip suggest that these slip systems are also activated during compression. In the final stage of plastic deformation, tension twin formation saturates, and grain orientation gradually stabilizes. According to the phenomenon of sharp increase in dislocation density again in the final deformation stage (Fig. 10(b)), it suggests that plastic deformation is gradually dominated by dislocations again.

4.2. Tension-compression asymmetry

The extruded alloy exhibits a tensile yield strength of 320 MPa, a UTS of 324 MPa, and a FE of 12.2% (Fig. 4(a)). The compressive yield strength is 236 MPa, the ultimate compressive strength is 432 MPa, and the strain is 11.3% (Fig. 9(a)). The alloy begins to yield at a strain of 1.2% under both tension and compression. Notably, the CYS/TYS ratio is 0.74, indicating distinct differences in the yield behavior under tensile and compressive loading. Fig. 4(c and d) and Fig. 9(c and d) show that the yielding crystal plane exhibits less lattice strain in compression compared to tension, which aligns with the phenomenon where CYS is lower than TYS.

The above results suggest a fiber texture in the alloy, with c-axes mainly aligned perpendicular to the loading direction. During tension, the easiest activated basal ⟨a⟩ slip system has a hard orientation with a low Schmid factor. Activating the basal ⟨a⟩ slip requires a higher load, thereby increasing the yield strength. When basal ⟨a⟩ slip is hard to activate, the early activation of low-CRSS tensile twinning becomes key. This can lower the yield strength if tensile twinning starts at low stress. Fig. 12(b) shows that profuse tensile twins are present in the compressed sample. It can be attributed to the lower CRSS required for tensile twinning, making it easier to be activated during compression loading. In contrast, as shown in Fig. 7, the extruded alloy exhibited few tension twins after tensile testing. Tensile twins are hard to initiate when compressive stress is applied along the grain's c-axis. Furthermore, twinning initiation is also significantly reduced due to the alloy's fine grain size [61]. The extensive activation of tension twins with lower CRSS results in a lower yield strength under compression. The activation of tension twins can cause grain rotations of 86°, leading to significant changes in the orientation of grains affected by these twins [62]. The compressed alloy's maximum texture intensity reaches 52.61, showing a strong texture, while Fig. 3(d) and Fig. 7(c) indicate little change in texture distribution and intensity after tension.

The activation of $\{10\bar{1}2\}$ tensile twinning can promote strain hardening of the sample through texture hardening and the Hall-Petch effect caused by grain refinement [63,64]. The extensive activation of tension twins contributes to the formation of a strong texture in the alloy, which re-orients the grains into hard orientations [65–67]. It becomes challenging for plastic deformation to proceed via basal slip. The primary deformation mechanisms of the grains involve the glide pyramidal I and II slip systems [68]. Fig. 7(d) and Fig. 12(d) show that the Schmid factors of non-basal ⟨a⟩ and ⟨c + a⟩ slips after compression are lower than that of the tensile sample, indicating that higher stress is required to activate them. Consequently, these tensile twins formed during compression inhibit the activation of slip, making it more difficult for the grains to slip and deform [69]. This inhibition leads to a higher SHR during compression.

In typical AZ-series Mg alloys, tensile twinning is readily activated under both tension and compression, which results in relatively low yield asymmetry [70]. In contrast, the studied alloy shows a much higher tensile yield strength and lower compressive yield strength, leading to more pronounced asymmetry. This distinct behavior originates from the fine-grained microstructure, which suppresses twinning during tension but still allows its extensive activation during compression. Compared with ultrafine-grained Mg alloys (e.g., with grain sizes of ~0.5 μm [33], where twinning is suppressed

even in compression and thus yield asymmetry is reduced, the present alloy represents an intermediate state with exceptionally large tensile–compressive asymmetry. Specifically, while grain refinement is sufficient to suppress twinning in tension, it is not fine enough to inhibit twinning in compression, thereby resulting in an exceptionally large degree of tensile–compressive yield asymmetry.

4.3. Strain hardening mechanisms

During tension, the SHR drops sharply after yielding, even reaching negative values, and then slightly increases, indicating the occurrence of softening behavior in the early stage (Fig. 4(b)). Tensile deformation is primarily accommodated by dislocation slip, especially basal slip. However, due to the scarcity of slip systems in hcp crystals, the overall plasticity is inherently restricted. In contrast, during compression, the SHR increases significantly after yielding and reaches a peak of approximately 5600 MPa at around 6.8% strain (Fig. 9(b)). In this case, $\{10\bar{1}2\}$ tensile twinning is rapidly activated, particularly in the early stages (before ~6.8% strain). This is consistent with previous studies, which have shown that in cases of single-peak strain hardening, $\{10\bar{1}2\}$ twinning is typically exhausted at around 6.8% strain, corresponding to the peak observed in the strain hardening curve [71]. The activation of twinning introduces extra deformation mechanisms and leads to pronounced crystallographic reorientation, which enhances SHR and promoting further deformation by reorienting grains in favor of basal and non-basal slip activation [72,73]. In addition, twin boundaries act as effective barriers to dislocation motion, increasing strain hardening and resulting in the continuous increase of the SHR [74].

Twinning and dislocation slips are both activated during compression and contribute to the increase in true stress. Therefore, their specific contributions to strain hardening can be quantified. Many previous studies have successfully employed the classical superposition principle to estimate the flow stress of metals under large elastoplastic deformation [75,76], and we follow this widely accepted methodology in the present work. The true stress is constructed by combining the contributions from solid-solution strengthening, grain boundary strengthening, precipitation strengthening, dislocation strengthening, and twinning strengthening. The true stress (σ) during compression can be estimated using the following equation [76]:

$$\sigma = \sigma_0 + \sigma_{ss} + \sigma_{gb} + \sigma_{ppt} + \sigma_{dis} + \sigma_{twin} \tag{6}$$

where σ_0 is the intrinsic lattice friction stress, σ_{ss} the contribution from solid solution strengthening, σ_{gb} grain boundary strengthening, σ_{ppt} precipitation strengthening, σ_{dis} dislocation strengthening (strain hardening or Taylor hardening), and σ_{twin} strengthening due to twinning. Among these, σ_0, σ_{ss}, σ_{gb} and σ_{ppt} remain essentially constant during deformation and are therefore treated additively, as is commonly done in yield strength calculations. Beyond yielding, the increase in true stress primarily originates from the evolution of dislocation density (σ_{dis}) and the activation of twinning (σ_{twin}), which progressively enhances the true stress. As a result, the true stress σ during compression can be expressed as:

$$\sigma = \sigma_y + \sigma_{dis} + \sigma_{twin} \tag{7}$$

where the σ_y is the yield strength which includes contributions from solid solution strengthening, grain boundary strengthening, precipitation strengthening, and initial dislocation strengthening, and $\Delta\sigma_{dis}$ is the strain hardening contribution from generated dislocations during compression. $\Delta\sigma_{dis}$ can be calculated using the Taylor formula:

$$\sigma_{dis} = M\alpha Gb\left(\sqrt{\rho} - \sqrt{\rho_0}\right) \tag{8}$$

where $M = 2.1$ as a representative Taylor factor for polycrystalline Mg alloys, $G = 16.6$ GPa as the shear modulus of Mg alloys, and $\alpha = 0.20$ as a constant commonly adopted in previous studies to account for the interaction strength among dislocations [77,78]. ρ_0 is the initial dislocation density, and ρ is the dislocation density during compression (Fig. 10(b)). Therefore, strengthening contribution from twinning (σ_{twin}) can be estimated by the difference between the true stress (σ) and $\sigma_y + \Delta\sigma_{dis}$ [63].

Fig. 14(a) shows the true stress increase from dislocations and twins during compression, and Fig. 14(b) displays these contributions as a percentage of true stress. Dislocations multiply rapidly after yielding, and the initial hardening is primarily attributed to dislocation activity. At a strain of approximately 5%, the contribution of dislocation hardening to the true stress reaches its peak value of 9.5%. In contrast, twinning contributes negligibly to hardening when the strain is below 5%. As the strain continues to increase, twins gradually expand, and their contribution to true stress rises sharply. At the point of failure, twinning hardening contributes 43% of the true stress.

Fig. 13 shows that twinning initiates immediately after yielding (at a strain of around 1.2%), and its volume fraction increases rapidly. However, its hardening effect does not become significant until the strain exceeds 5%. This indicates that while twins nucleate and grow shortly after yielding, they do not immediately contribute to hardening. In the early stages, twins may mainly act to accommodate deformation by reorienting the lattice rather than impeding dislocation motion. It is only when the twin boundaries become more widespread and start interacting with dislocations or other twins that they significantly contribute to the material's resistance to deformation, thereby contributing to strain hardening. In the later stage (after a strain of 8%), the twin volume fraction remains nearly constant (Fig. 13). However, the hardening effect induced by twinning continues to increase during this stage (Fig. 14). This can be attributed to enhanced interactions between twins and dislocations, increased obstruction of dislocation motion by twin boundaries. As a result, it can be concluded that the hardening effect induced by twinning primarily originates from the formation of twin boundaries, which act as practical barriers to dislocation motion. These boundaries hinder dislocation glide and accumulation, thereby enhancing the strain-hardening behavior. This is consistent with previous studies [79], which reported that the strength-

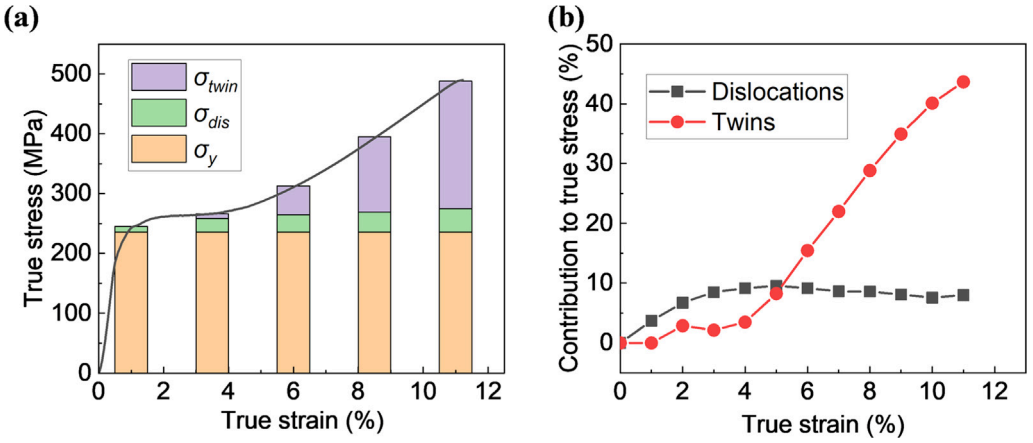

Fig. 14. (a) Dislocation and twinning contributions to true stress increase during compression. (b) Relative strengthening effects of dislocations and twinning, expressed as percentages of true stress.

ening role of twinning arises primarily from the barriers imposed by twin boundaries against dislocation motion rather than from twin nucleation itself. Similar to their conclusions, we also observe that the twin volume fraction saturates in the later stages of compression, but the hardening contribution of twinning continues to increase due to sustained twin–dislocation interactions. More recently, Li et al. [63] emphasized that the hardening contribution of twinning in Mg alloys is highly complex, involving multiple mechanisms. Specifically, they reported that lenticular-shaped twins can effectively subdivide grains and trigger a dynamic Hall–Petch effect, while long-range back stresses from dislocation pileups near twin boundaries and short-range basal–prismatic dislocation transmutation provide additional, albeit limited, contributions. Despite a twin volume fraction approaching ~40%, they found that dislocations remained the dominant hardening mechanism. Our results provide a clear explanation for this phenomenon, showing that the strengthening effect is not directly correlated with twin volume fraction. Instead, only after the twin boundaries become sufficiently developed do they begin to strongly interact with dislocations, leading to a marked increase in hardening. Compared with existing studies, our work thus provides new quantitative evidence that the onset and saturation of twinning volume fraction are temporally decoupled from its strengthening effect, thereby deepening the mechanistic understanding of twin–dislocation interactions in fine-grained Mg alloys. In addition, Fig. 14 shows that twinning contributes up to 43% of the true stress in the late stage of compression, while dislocation glide remains the primary carrier of plastic deformation. As indicated in Fig. 13, tensile twinning initiates in the early stage of deformation, but its hardening effect becomes significant only after sufficient twin boundaries are formed. In the later stage, although the twin volume fraction saturates, these boundaries increasingly impede dislocation motion, leading to sustained strengthening. Thus, the high twinning contribution does not imply a replacement of dislocation slip, but rather reflects strong twin–dislocation interactions, with twin boundaries acting as effective barriers that enhance strain hardening.

5. Conclusion

In this study, we have investigated the tension-compression asymmetry and related plastic deformation mechanisms of an extruded Mg-0.6Mn-0.5Al-0.5Zn-0.4Ca alloy using in-situ tensile and compressive tests while performing synchrotron X-ray diffraction. The main conclusions are as follows:

(1) The lattice strains during tension and compression are significantly influenced by the initial texture. During tension, grain orientation remains nearly unchanged, resulting in stable lattice strain on different planes. In contrast, the {0002} planes of most grains shift from being parallel to being perpendicular to the loading direction during compression, with lattice strain evolving according to the preferred orientation.
(2) Both tension and compression induced the significant activation and proliferation of dislocations. Slip is the dominant deformation mechanism during tension, with extensive activation of non-basal ⟨a⟩ and ⟨c + a⟩ slips, while deformation twinning is suppressed. During compression, tensile twinning dominates early plastic deformation, while dislocation slips dominate later stages.
(3) The alloy shows tension-compression asymmetry (CYS/TYS = 0.74). During compression, tensile twinning is more readily activated, reducing the yield strength. Basal ⟨a⟩ slip requires a higher stress to be activated during tension, but it is easier to be activated during compression due to a higher Schmid factor.
(4) During tension, the strain hardening rate (SHR) drops sharply after yielding due to limited available slip systems and grain boundary sliding. In contrast, compression exhibits a significant increase in SHR after yielding, primarily driven by twin boundary formation, texture evolution, and dislocations multiplication, with twinning playing a dominant role at higher strains.
(5) Dislocation multiplication dominates the initial strain hardening during compression, while twinning progressively contributes more significantly to the plastic deformation

at higher strains. At failure, twinning accounts for approximately 43% of the true stress, demonstrating that twin boundaries serve as crucial barriers to dislocation motion and are the primary source of strain hardening at later deformation stages.

Declaration of competing interest

Yuanding Huang and Yan Yang are editorial board members/editor-in-chief for Journal of Magnesium and Alloys and was not involved in the editorial review or the decision to publish this article. All authors declare that there are no competing interests.

CRediT authorship contribution statement

Hao Chen: Writing – original draft, Methodology, Investigation, Data curation. **Huicong Chen:** Writing – review & editing. **Yuanding Huang:** Writing – review & editing, Supervision, Resources, Methodology. **Weimin Gan:** Writing – review & editing, Resources, Methodology. **Emad Maawad:** Writing – review & editing. **Weidong Xie:** Supervision, Project administration, Funding acquisition. **Guobing Wei:** Supervision, Funding acquisition. **Yan Yang:** Funding acquisition. **Yu Zou:** Writing – review & editing, Supervision.

Acknowledgments

H. C. thanks DESY (Hamburg, Germany), part of the Helmholtz Association HGF, for providing experimental facilities. This research partly took place at PETRA III, and H. C. appreciates Dr. Norbert Schell's help with beamline P07B.

References

[1] Y. Yang, J. Wang, M.R.G. Ferdowsi, S.R. Kada, T. Dorin, M.R. Barnett, M. Perez, Acta Mater. 281 (2024) 120392.
[2] Q. Li, L. Jin, F. Wang, S. Dong, J. Zeng, F. Wang, J. Dong, Int. J. Plas. 190 (2025) 104367.
[3] Y. Yang, X. Xiong, J. Chen, X. Chen, X. Peng, F. Pan, J. Magnes. Alloys 13 (5) (2025) 1855–1858.
[4] S.S. Dash, R.C. Fernandes, X. Shang, Y. Zou, H. Peng, X. Jiang, X. Fang, N. Ma, D. Li, D. Chen, J. Magnes. Alloys 13 (5) (2025) 1939–1952.
[5] J. Li, Q. Han, X. Han, X. Yi, J. Magnes. Alloys 12 (11) (2024) 4709–4721.
[6] F.-F. Li, G. Fang, Int. J. Plast. 152 (2022) 103258.
[7] C.M.A. Iftikhar, A. Brahme, K. Inal, A.S. Khan, Int. J. Plast. 151 (2022) 103216.
[8] L. Zhou, G. Ren, T. Huang, Z. Wang, F. Wang, Z. Wei, P. Mao, Z. Liu, J. Magnes. Alloys 13 (5) (2025) 2358–2373.
[9] Q. Yang, S. Lv, P. Chen, Z. Xie, S. Zhou, X. Qiu, J. Magnes. Alloys 13 (2) (2025) 583–591.
[10] T. Zhou, B. Wang, Y. Li, S. Hu, X. Li, D. Liu, J. Mater. Sci. Technol. 199 (2024) 222–245.
[11] W. Chen, W. He, B. Jiang, F. Pan, Int. J. Plast. 170 (2023) 103753.
[12] H. Chen, C. Shao, L. Wang, H. Chen, Y. Zou, J. Magnes. Alloys 13 (4) (2025) 1549–1560.
[13] T. Zhou, Y. Li, F. Guo, Q. Li, Z. Jia, D. Liu, J. Magnes. Alloys 12 (11) (2024) 4622–4645.
[14] T. Wang, M. Zha, Y. Gao, S.-Q. Wang, H.-L. Jia, C. Wang, H.-Y. Wang, Int. J. Plast. 170 (2023) 103766.
[15] M. Kavyani, G.R. Ebrahimi, H.R. Ezatpour, M. Jahazi, J. Magnes. Alloys 10 (6) (2022) 1640–1662.
[16] X. Huang, Y. Xin, Y. Cao, W. Li, G. Huang, X. Zhao, Q. Liu, P. Wu, Int. J. Plast. 158 (2022) 103412.
[17] H. Zhan, J. Zhang, J. Miao, C. Wang, G. Zeng, J. Wang, A.A. Luo, Mater. Sci. Eng. A 897 (2024) 146321.
[18] M.Q. Zhang, T. Nakata, C. Xu, G.Z. Tang, K.K. Deng, X.J. Wang, G.S. Wang, S. Kamado, L. Geng, J. Magnes. Alloys (2024).
[19] H.M.R. Tariq, U.M. Chaudry, M. Ishtiaq, M. Kim, M. Ali, T.-S. Jun, J. Magnes. Alloys 12 (11) (2024) 4694–4708.
[20] X. Huang, M. Bian, I. Nakatsugawa, Y. Chino, M. Sato, K. Yamazaki, F. Kido, H. Ueda, M. Inoue, J. Alloys Compd. 887 (2021) 161394.
[21] K. Kikuchi, T. Nakata, Z.H. Li, T.T. Sasaki, Y. Miyashita, S. Kamado, J. Alloys Compd. 1027 (2025) 180504.
[22] H. Yeganeh, A. Bahmani, M. Lotfpour, M. Malekan, M. Emamy, B. Nayebi, K.S. Shin, J. Magnes. Alloys 11 (4) (2023) 1276–1291.
[23] T.-S. Wang, Z.-M. Hua, C. Wang, M. Zha, Y. Gao, H.-Y. Wang, J. Magnes. Alloys 12 (10) (2023) 4085–4095.
[24] R. Ni, H. Liu, S. Hua, H. Zhou, Y. Zeng, D. Yin, J. Magnes. Alloys 13 (8) (2024) 3880–3895.
[25] J. Li, H. Chen, D. Wu, R. Chen, J. Song, X. Yi, J. Mater. Sci. Technol. 219 (2025) 134–146.
[26] B. Yang, J. Wang, Y. Li, M. Barnett, J. Llorca, Acta Mater. 248 (2023) 118766.
[27] X. Zheng, R. Ni, Z. Jiang, H. Zhou, Y. Zeng, D. Yin, Mater. Sci. Eng. A 920 (2025) 147533.
[28] Q. Yang, S. Lv, Z. Yan, Z. Xie, X. Qiu, J. Magnes. Alloys 12 (2) (2024) 687–699.
[29] D.D. Yin, C.J. Boehlert, L.J. Long, G.H. Huang, H. Zhou, J. Zheng, Q.D. Wang, Int. J. Plast. 136 (2021) 102878.
[30] Y. Han, S. He, T. Chen, J. Shao, C. Liu, Z. Chen, Z. Yang, Mater. Sci. Eng. A 856 (2022) 144002.
[31] L. Xiao, G. Yang, C. Wang, J. Chen, W. Jie, Materi. Sci. Eng. A 883 (2023) 145514.
[32] R. Ni, Z. Jiang, C. Boehlert, J. Zheng, H. Zhou, Q. Wang, D. Yin, Int. J. Plast. 189 (2025) 104354.
[33] X. Liu, X. Qiao, X. Zhang, D. Zhang, L. Xiao, W. Zhong, X. Zhu, J. Lian, M. Zheng, J. Mater. Res. Technol. 28 (2024) 2235–2246.
[34] J.J. Bhattacharyya, S. Faberman, A. Sullivan, M. Saha, T. Sasaki, S.R. Agnew, Scr. Mater. 262 (2025) 116659.
[35] L. Wang, H.-L. Yan, Y. Zhang, B. Beausir, W. Gan, P. Laurent, N. Siredey-Schwaller, C. Esling, X. Zhao, L. Zuo, Int. J. Plast. 186 (2025) 104260.
[36] H. Chen, L. Lang, X. Shang, S.S. Dash, Y. He, G. King, Y. Zou, Acta Mater. 271 (2024) 119885.
[37] T. Masumura, K. Inami, K. Matsuda, T. Tsuchiyama, S. Nanba, A. Kitahara, Acta Mater. 234 (2022) 118052.
[38] A. Borbély, Scr. Mater. 217 (2022) 114768.
[39] T. Ungar, S. Ott, P.G. Sanders, A. Borbely, J.R. Weertman, Acta Mater. 46 (10) (1998) 3693–3699.
[40] T. Ungár, I. Dragomir, A. Révész, A. Borbély, J. Appl. Crystallogr. 32 (1999) 992–1002.
[41] D. Balzar, H. Ledbetter, J. Appl. Crystallogr. 26 (1993) 97–103.
[42] H. Chen, C. Hu, F. Hu, X. Liu, F. Kong, W. Xie, G. Wei, Y. Yang, X. Peng, Y. Huang, N. Hort, Mater. Charact. 196 (2023) 112575.
[43] H. Chen, L. Sun, X. Ke, F. Kong, W. Xie, G. Wei, Y. Yang, X. Peng, Mater. Sci. Eng. A 858 (2022) 144117.
[44] S. Zhou, T. Liu, A. Tang, Y. Huang, P. Peng, J. Zhang, N. Hort, R. Willumeit-Römer, F. Pan, Mater. Des. 225 (2023) 111476.
[45] Z.Y. Zhong, H.G. Brokmeier, E. Maawad, N. Schell, Mater. Sci. Eng. A 639 (2015) 519–525.
[46] Z.Y. Zhong, H.G. Brokmeier, W.M. Gan, E. Maawad, B. Schwebke, N. Schell, Mater. Charact. 108 (2015) 124–131.
[47] T. Ungár, L. Li, G. Tichy, W. Pantleon, H. Choo, P.K. Liaw, Scr. Mater. 64 (9) (2011) 876–879.
[48] K. Nakagawa, M. Hayashi, K. Takano-Satoh, H. Matsunaga, H. Mori,

K. Maki, Y. Onuki, S. Suzuki, S. Sato, Quant. Beam Sci. 4 (4) (2020) 36.
[49] M. Griffiths, D. Sage, R.A. Holt, C.N. Tome, Metall. Mater. Trans. A 33 (3) (2002) 859–865.
[50] H. Somekawa, R. Ueji, A. Singh, Mater. Sci. Eng. A 897 (2024) 146319.
[51] P.C. Gautam, S. Biswas, J. Magnes. Alloys 12 (11) (2024) 4646–4666.
[52] Q.H. Zhang, X.H. Zhang, X.J. Yang, M. Huang, Appl. Sci. Basel 15 (3) (2025) 1571.
[53] H.J. Pan, Y. He, X.D. Zhang, Materials (Basel) 14 (4) (2021) 1012.
[54] S.K. Sahoo, S. Biswas, L.S. Toth, P.C. Gautam, B. Beausir, Int. J. Plast. 128 (2020) 102660.
[55] X. Luo, Z. Feng, T. Yu, J. Luo, T. Huang, G. Wu, N. Hansen, X. Huang, Acta Mater. 183 (2020) 398–407.
[56] X. Luo, X. Wang, Y. Xia, G. Wu, Y. Cheng, T. Yu, P. Yan, Y. Xin, X. Huang, J. Mater. Sci. Technol. 226 (2024) 290–301.
[57] X. Zhang, R. Zhou, C. Li, H. Yue, Q. Chen, J. Magnes. Alloys 13 (6) (2024) 2800–2812.
[58] L. He, J. Zheng, M. Xu, T. Li, D. Yin, B. Jiang, F. Pan, H. Zhou, Int. J. Plast. 183 (2024) 104160.
[59] Y. Chen, A. Li, X. Kong, Z. Ma, G. Kang, D. Jiang, K. Zhao, Y. Ren, L. Cui, K. Yu, Acta Mater. 236 (2022) 118131.
[60] F. Wang, Y. Gu, R.J. McCabe, L. Capolungo, J.A. El-Awady, S.R. Agnew, Acta Mater. 195 (2020) 13–24.
[61] K. Wei, R. Hu, D.D. Yin, L.R. Xiao, S. Pang, Y. Cao, H. Zhou, Y.H. Zhao, Y.T. Zhu, Acta Mater. 206 (2021) 116604.
[62] A.H. Zahiri, E. Vitral, J. Ombogo, M. Lotfpour, L. Cao, Acta Mater. 241 (2022) 118377.
[63] M.-Y. Li, Z.-P. Guan, P. Chen, M.-W. Ren, G. Wang, W. Yan, P. Zhao, J.-W. Song, Mater. Des. 239 (2024) 112770.
[64] Z. Zhang, L. Yuan, M. Zheng, D. Shan, B. Guo, Mater. Sci. Eng. A 859 (2022) 144185.
[65] H.-H. Lu, L. Lu, W. Liang, Mater. Sci. Eng. A 862 (2023) 144472.
[66] G. Proust, C.N. Tomé, A. Jain, S.R. Agnew, Int. J. Plast. 25 (5) (2009) 861–880.
[67] B. Clausen, C.N. Tomé, D.W. Brown, S.R. Agnew, Acta Mater. 56 (11) (2008) 2456–2468.
[68] T. Zhao, Y. Hu, Y. Wang, Y. Dai, T. Zheng, Z. Li, K. Li, B. He, C. Zhang, F. Pan, J. Magnes. Alloys 13 (7) (2023) 3150–3165.
[69] D.K. Chouhan, S. Mondal, B. Bhattacharya, S. Biswas, Int. J. Plast. 161 (2023) 103516.
[70] D.L. Zhong, N.B. Zhang, S. Chen, Y.Y. Zhang, Z.L. Li, H.L. Xie, L. Lu, X.L. Gong, S.N. Luo, Mater. Sci. Eng. A 826 (2021) 141987.
[71] B. Guan, L. Wang, Y. Xin, P. Wu, J. Xu, X. Huang, Q. Liu, Int. J. Plast. 179 (2024) 104041.
[72] N. Li, L. Yang, C. Wang, M.A. Monclús, D. Shi, J.M. Molina-Aldareguía, Mater. Sci. Eng. A 819 (2021) 141408.
[73] C.S. Hyun, J. Singh, M. Panchal, M.S. Kim, A. Komissarov, K.S. Shin, S.H. Choi, Int. J. Plast. 184 (2025) 104198.
[74] Z. Wang, X. Zhao, S. Li, J. Yu, J. Mater. Res. Technol. 29 (2024) 3656–3672.
[75] Z.Y. Liang, Y.Z. Li, M.X. Huang, Scr. Mater. 112 (2016) 28–31.
[76] Y.Z. Li, Z.Y. Liang, M.X. Huang, Int. J. Plast. 150 (2022) 103198.
[77] Y. Wan, B. Tang, Y. Gao, L. Tang, G. Sha, B. Zhang, N. Liang, C. Liu, S. Jiang, Z. Chen, X. Guo, Y. Zhao, Acta Mater. 200 (2020) 274–286.
[78] H. Chen, Y. Yang, F. Hu, X. Liu, F. Kong, X. Cui, W. Xie, G. Wei, Y. Yang, X. Peng, Y. Huang, Mater. Sci. Eng. A 865 (2023) 144629.
[79] H. El Kadiri, J. Kapil, A.L. Oppedal, L.G. Hector, S.R. Agnew, M. Cherkaoui, S.C. Vogel, Acta Mater. 61 (10) (2013) 3549–3563.